Journal of Materials Science & Technology 164 (2023) 150–159

Contents lists available at ScienceDirect

Journal of Materials Science & Technology

journal homepage: www.elsevier.com/locate/jmst

Research Article

Wafer-scale heterogeneous integration of self-powered lead-free metal halide UV photodetectors with ultrahigh stability and homogeneity

Ming Deng[a], Ziqing Li[b,*], Xiaolei Deng[a], Ying Hu[a], Xiaosheng Fang[a,b,*]

[a] Department of Materials Science, State Key Laboratory of Molecular Engineering of Polymers, Fudan University, Shanghai 200433, China
[b] Shanghai Frontiers Science Research Base of Intelligent Optoelectronics and Perception, Institute of Optoelectronics, Fudan University, Shanghai 200433, China

ARTICLE INFO

Article history:
Received 24 April 2023
Revised 16 May 2023
Accepted 17 May 2023
Available online 2 June 2023

Keywords:
Photodetector
Lead-free metal halide
Wafer-scale
Vacuum evaporation
Imaging sensor

ABSTRACT

Large-scale growth and heterogeneous integration with existing semiconductors are the main obstacles to the application of metal halide perovskites in optoelectronics. Herein, a universal vacuum evaporation strategy is presented to prepare copper halide films with wafer-scale spatial homogeneity. Benefiting from the electric field manipulation method, the built-in electric fields are optimized and further boost the self-powered UV photodetecting performances of common wide-bandgap semiconductors by more than three orders of magnitude. Furthermore, with effective modulation of the interfacial charge dynamics, the as-fabricated GaN-substrate heterojunction photodetector demonstrates an ultrahigh on/off ratio exceeding 10^7, an impressive responsivity of up to 256 mA W^{-1}, and a remarkable detectivity of 2.16×10^{13} Jones at 350 nm, 0 V bias. Additionally, the device exhibits an ultrafast response speed (t_r/t_d = 716 ns/1.30 ms), an ultra-narrow photoresponse spectrum with an FWHM of 18 nm and outstanding continuous operational stability as well as long-term stability. Subsequently, a 372-pixel light-powered imaging sensor array with the coefficient of variation of photocurrents reducing to 5.20% is constructed, which demonstrates exceptional electrical homogeneity, operational reliability, and UV imaging capability. This strategy provides an efficient way for large-scale integration of metal halide perovskites with commercial semiconductors for miniature optoelectronic devices.

© 2023 Published by Elsevier Ltd on behalf of The editorial office of Journal of Materials Science & Technology.

1. Introduction

In the Internet of Things era, electronics keep developing towards portability, miniaturization, and energy-conservation. Tremendous efforts have been made in developing low-power consumption devices capable of working independently, stably, and continuously without external power sources [1,2]. Recent decades have witnessed the dramatic prosperity of ultraviolet photodetectors (UV PDs) in military reconnaissance, medical diagnosis, aerospace exploration, environmental monitoring, and other fields. And numerous inorganic semiconductors with large bandgap and strong UV absorption, including Ga_2O_3, TiO_2, ZnO, and GaN, have flourished in the manufacture of UV PDs for miniature and portable electronics [3–6]. However, research towards heterogeneous integration and interface engineering still needs further exploring to achieve a balance between high responsivity and fast response speed. In this context, schemes of electric field manipulation that can regulate the behavior and transportation of carriers have been proposed, including the manipulation of gate voltage field, photogating field, ferroelectric field, and built-in electric field [7,8]. Through these means, the photodetecting capability of a PD can be optimized by facilitating carrier separation, reducing charge recombination, and suppressing majority carrier diffusion, consequently endowing the photodetector with ultra-low dark current and fast response speed [9,10]. Constructing heterojunctions between semiconductors with intrinsically different nature is a prevalent strategy to design built-in electric fields [11–13]. The fabrication and optimization of built-in electric fields with heterostructure materials provide a robust force to modulate carrier transmission and have emerged as a state-of-the-art frontier for manipulating interfacial charge dynamics.

As a promising candidate for optoelectronic semiconductors, lead-based halide perovskites demonstrate component adjustability and excellent optoelectronic properties, such as adjustable bandgap, long carrier lifetime, high carrier mobility, and so on [14,15]. Nevertheless, the lead toxicity and instability have severely obstructed their further application and large-scale commercialization [16–18]. Therefore, lead-free perovskites such as Cu- [19],

* Corresponding authors.
E-mail addresses: lzq@fudan.edu.cn (Z. Li), xshfang@fudan.edu.cn (X. Fang).

https://doi.org/10.1016/j.jmst.2023.05.007
1005-0302/© 2023 Published by Elsevier Ltd on behalf of The editorial office of Journal of Materials Science & Technology.

Bi- [20], Sb- [21], Sn- [22], and Ge-based [23] perovskites have become hotspots in environmental-friendly photodetector applications. While Sn- and Ge-based perovskites suffer from oxidation problems, Bi- and Sb-based perovskites exhibit low carrier mobility and weak responsivity, Cu-based halide perovskite derivatives (e.g. $CsCu_2I_3$ and $Cs_3Cu_2I_5$) have emerged and been widely utilized in optoelectronic applications, owing to their decent optoelectrical properties, low toxicity, high stability, and abundant source [24–28].

The technology for the preparation of high-quality metal halide perovskite thin films has always been the key point to realizing high-performance devices. Solution-processed methods like spin-coating and colloidal synthesis are most commonly used to prepare perovskite films [19,24,29–31], but the fact that organic solvents may affect surface planeness remains an inevitable problem. The vacuum evaporation method, meanwhile, provides an important way to grow films with high purity, fewer defects, and homogeneous morphology, and exhibits the advantages of mature construction facilities, solvent-free green processing, etc. [32,33]. The substrate-independent nature and high controllability of film thickness also endow the vacuum evaporation technology with great promise for reproducible and reliable experiments [34]. More importantly, it has proven to be an effective method for industrial large-scale production [35]. At present, few pieces of research have been carried out on the vacuum deposition of perovskite films, especially in the applications of photodetectors. Intriguingly, for Cs-Cu-I films, the adopted precursors by vacuum-thermal evaporation are inorganic minerals (CsI and CuI) with similar properties, which avoids the problems caused by the distinct properties of common organometallic perovskite precursors [33].

This paper aims to prepare wafer-scale Cs-Cu-I thin films with high uniformity and planeness via vacuum-thermal evaporation technology. The as-prepared metal halide perovskite thin films are introduced to manipulate electric fields and boost the self-powered performance, including dramatically decreased dark current, ultra-high on/off ratio, remarkable wavelength selectivity, and outstanding stability. Furthermore, the fabricated 372-pixel imaging array exhibits excellent electrical homogeneity, high consistency, and decent imaging functionality. The experimental results indicate the promising potential of vacuum-deposited heterogeneous integration of metal halide perovskites and wide-bandgap semiconductors for high-performance UV imaging technology.

2. Experimental section

2.1. Preparation of GaN substrate and TiO_2 film

Square GaN substrate (1 cm × 1 cm) is cut from a commercially available n-GaN wafer (purchased from Dongguan Sino Nitride Semiconductor Co., Ltd, with a thickness of 4.5 ± 0.5 µm, a resistivity ≤ 0.5 Ω cm, a carrier concentration ≤ 5 × 10^{17} cm^{-3}) and washed with acetone, anhydrous ethanol, and deionized water for 10 min each. TiO_2 film was prepared by traditional sol-gel method and spin-coating process. First, TiO_2 precursor was prepared. 1 mL of tetrabutyl titanate (Aladdin Chemistry Co., Ltd., 99%) was dissolved in 9 mL of anhydrous ethanol. Then, 1 mL of acetic acid was added dropwise to the solution and stirred for 30 min. Furthermore, 1 mL of acetylacetone (Aladdin Chemistry Co., Ltd., 99%) was added dropwise to the solution and stirred for 30 min. Additionally, 1 mL of deionized water was added dropwise to the solution and stirred for 30 min. Finally, the solution was aged for 12 h to obtain the precursor. Quartz substrate was washed with acetone, anhydrous ethanol, and deionized water for 10 min each, and hydrophilized with plasma for 3 min before use. A drop of TiO_2 precursor was dropped on the surface of the quartz, spin-coating at 500 rpm for 6 s, and then 3000 rpm for 30 s. After spin-coating, it was placed on the hot plate and baked at 90 °C for 10 min. Finally, the whole substrate was transferred to a muffle furnace for thermal annealing. The furnace temperature was raised to 550 °C within 8 h and maintained at 550 °C for 1 h, and then air-cooled to room temperature.

2.2. Vapor evaporation of Cs-Cu-I films

Cs-Cu-I nanoscale films were grown by the vacuum-thermal evaporation method. A total of CsI (Aladdin Chemistry Co., Ltd., 99.999%) and CuI (Aladdin Chemistry Co., Ltd., 99.95%) were mixed and thoroughly ground in an agate mortar, and the obtained fine powder was put into a quartz boat as the evaporation source. In order to prepare $CsCu_2I_3$ and $Cs_3Cu_2I_5$, the mass ratios of the pristine materials CsI and CuI were 0.2598 g: 0.3808 g (molar ratio 1: 2) and 0.7794 g: 0.3808 g (molar ratio 3: 2), respectively. Then a mask was fixed on the surface of the TiO_2 or GaN substrate, and the whole was fixed on the top of the evaporation chamber. After evacuating the vacuum chamber to a pressure of below 5 × 10^{-4} Pa, the evaporation source was heated to deposit 30 nm Cs-Cu-I film on the substrate at the deposition rate of 0.3 Å s^{-1}, then increase the deposition rate to 1 Å s^{-1} and continue to deposit the film to a thickness of 250 nm. And the proposed reactions processes are as follows:

$$CsI + 2CuI \rightarrow CsCu_2I_3 \quad (1)$$

$$3CsI + 2CuI \rightarrow Cs_3Cu_2I_5 \quad (2)$$

2.3. Fabrication of devices

After the deposition of Cs-Cu-I, there will be a straight boundary between Cs-Cu-I and TiO_2 or GaN due to the existence of the complete mask. Silver pastes were dipped onto both sides of the boundary as two electrodes of PDs. The distance between them is sub-millimeter level. Then, Ag-TiO_2(GaN)-$CsCu_2I_3$($Cs_3Cu_2I_5$)-Ag photodetectors were fabricated. It should be noted that in order to construct Ag-GaN–$CsCu_2I_3$-Au photodetector, after $CsCu_2I_3$ was deposited on GaN (using a mask with square cutouts with the size of 0.5 mm × 0.5 mm), Au with the thickness of 50 nm was directly and continuously evaporated on $CsCu_2I_3$ as an electrode, followed by dipping a silver paste next to the square Au electrode formed on GaN. The two electrodes formed a pair of asymmetric electrodes. The structures of common composite system devices and the Ag-GaN–$CsCu_2I_3$-Au device are shown in Fig. S1 in Supporting Information, respectively.

2.4. Fabrication of high-performance UV imaging device

A whole GaN wafer with a diameter of 5.2 cm was washed with acetone, anhydrous ethanol, and deionized water for 10 min each. A customized mask with 600 (30 rows & 20 columns) pairs of square notches (0.5 mm × 0.5 mm) was fixed on the GaN surface as shown in Fig. 1(a). One of each pair of notches was covered with heat-resistant tape on the mask. Then the $CsCu_2I_3$ was evaporated on it through the steps described in Experimental section 2.2, and only the $CsCu_2I_3$ passing through the uncovered notches can reach the surface of GaN. Then remove the tape and continue to evaporate 100 nm Au which can reach the surface of GaN through all notches and function as electrodes. Then, a wafer-scale photodetector array with 372 pixels is prepared.

2.5. Characterization and measurements

Optical photographs were taken with Olympus optical microscope. Surface morphologies of the samples were obtained by field

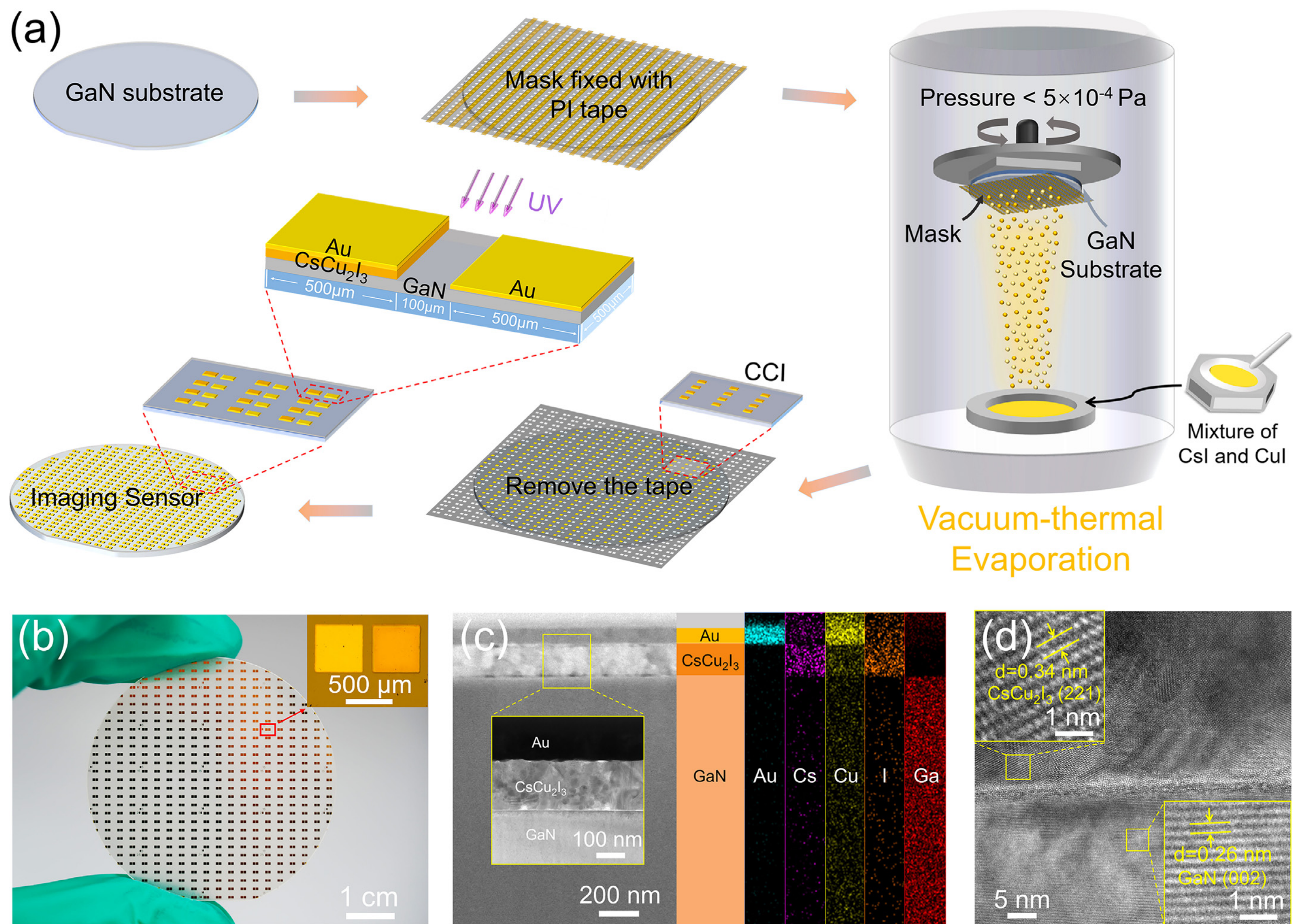

Fig. 1. The GaN–$CsCu_2I_3$ photodetector arrays fabricated by the wafer-scale vacuum-thermal evaporation method. (a) Schematic diagram of the fabrication process. (b) Photograph of the 2-inch 372-pixel imaging sensor, inset is an optical microscope image of the single pixel unit. (c) Left panel: cross-section TEM image of the $CsCu_2I_3$ film on the GaN wafer, inset is the enlarged TEM image showing the Au/$CsCu_2I_3$/GaN interfaces. Middle panel: schematic illustration of a cross-section of the as-grown $CsCu_2I_3$ film on the GaN wafer. Right panel: EDS elemental mapping of the object elements. (d) High-resolution TEM image of the cross-section of the contacting interface between $CsCu_2I_3$ film (top) and GaN wafer (bottom).

emission SEM (Zeiss Sigma) and atomic force microscope (AFM, Bruker Dimension Icon). X-ray diffraction (XRD) patterns were obtained by a Bruker D8 Advance X-ray diffractometer equipped with Cu K_α radiation (λ = 1.5406 Å). The powder sample was tested with the scan step of 0.02° and a step time of 0.1 s. Focused-ion beam (FIB) measurement was conducted on FEI Scios 2 HiVac. Transmission electron microscopy (TEM) measurement was performed on FEI talos F200x G2. X-ray photoelectron spectra (XPS) were collected by the PHI5000C & PHI5300 X-ray photoelectron spectrometer, equipped with a dual Mg/Al anode. All peaks were calibrated using the C 1s peak (284.6 eV) as the reference, and the deconvolution was conducted using a Gaussian-Lorentzian fitting after background subtraction. Energy dispersive X-ray spectroscopy (EDS) was tested on EDS super-X. The absorption and transmittance spectra were characterized by a UV–Vis spectrophotometer (Hitachi U-4100). The Raman spectra were collected by a Raman system (XperRam-35 V) with a 532 nm laser. The semiconductor characterization system Keithley 4200-SCS with a light source system consisting of a continuous tunable 75 W Xe lamp and a monochromator was used for optoelectronic tests, like collecting the *I–V* and *I–t* characteristics. A NOVA II optical power meter (Ophir Photonics) was used to measure power density. The transient photoresponse data were collected by using a transient light response system with a Q-switch YAG: Nd laser (Continuum Electro-Optics, MINILITE II, pulse duration: 1 μs, 355 nm), a resistor and an oscilloscope (Tektronix MSO/DPO5000). The imaging process was conducted by measuring the current of illumination or non-illumination areas until all pixels were checked. All the above measurements were conducted under air atmosphere and room temperature.

3. Results and discussion

3.1. Device fabrication

The schematic diagram and step description of the detailed preparation process of single devices (on TiO_2 and GaN) and device arrays (on GaN wafer) are presented in Figs. 1(a) and S1 and Experimental section. By changing the composition proportion of CsI and CuI, large-area $CsCu_2I_3$ and $Cs_3Cu_2I_5$ nanoscale films can be successfully deposited onto substrates respectively to construct the material composite structure. Specifically, Fig. 1(a) illustrates the fabrication process of the device array, in which a customized mask with multiple pairs of square notches was applied to realize the patterning of $CsCu_2I_3$ and Au and to construct large-scale arrayed Au-$CsCu_2I_3$-GaN-Au devices. And the photograph of the array fabricated on a 2-inch GaN wafer is shown in Fig. 1(b). Fig. S2(a) depicts the XRD patterns of evaporated Cs-Cu-I films, and

the position and intensity of these signal peaks are in good agreement with those of crystal planes of the orthorhombic $CsCu_2I_3$ (Space group *Pbnm*, PDF No.45–0076) and $Cs_3Cu_2I_5$ (Space group *Cmcm*, PDF No.45–0077). Specifically, characteristic peaks located at 25.99° and 26.98° of $CsCu_2I_3$ can be assigned to (221) and (040) planes. And the characteristic peaks located at 25.49° and 26.23° of $Cs_3Cu_2I_5$ can be allocated to (312) and (222) planes, respectively. XPS was employed to analyze the chemical composition of the surface of Cs-Cu-I films (Fig. S2(b)). Apart from O 1 s and C 1 s peaks caused by absorbed contaminations, all peaks are attributed to the main constituent elements (Cs, Cu, and I) of $CsCu_2I_3$ and $Cs_3Cu_2I_5$ films, indicating the high purity of films prepared by the vacuum-thermal evaporation. And the detailed XPS data of the Cs 3d core level, Cu 2p core level, and I 3d core level are shown in Fig. S3, corresponding to previously reported studies [24,27]. The high purity can be ascribed to the strict circumstance with high vacuum degrees ($< 5 \times 10^{-4}$ Pa) during the vacuum-thermal evaporation process, which prevents the films from being exposed to impurities or being contaminated. The absorption spectra of $CsCu_2I_3$ and $Cs_3Cu_2I_5$ films are shown in Fig. S4.

FIB-prepared GaN–$CsCu_2I_3$ samples were utilized to display the microstructure of the contacting interface. As revealed in Fig. 1(c), the cross-section transmission electron microscopy (TEM) image shows the clear layered structure of Au/$CsCu_2I_3$/GaN/sapphire (from top to bottom) in the device, and the EDS mapping also indicates the high purity and homogeneous layered distribution of corresponding elements. Note that the detection of Cu and I elements was obviously interfered with by Au. Moreover, the high-resolution TEM image in Fig. 1(d) further displays the compact and large-area interfacial contact between the GaN and $CsCu_2I_3$ films, from which it can be observed that their interplanar spacings are 0.26 and 0.34 nm, corresponding to GaN (002) and $CsCu_2I_3$ (221) crystal planes, respectively. Fig. S5 depicts the $CsCu_2I_3$/Au interface and the selected-area electron diffraction (SAED) patterns of the GaN wafer and the $CsCu_2I_3$/GaN interface. It is obvious that the SAED pattern of single crystal GaN shows regular diffraction points, while that of the $CsCu_2I_3$/GaN interface reveals typical diffraction rings of polycrystalline. The atomically sharp and uniform interface between GaN and $CsCu_2I_3$ indicates that there are no obvious gaps, defects, or contamination, resulting in efficient charge transmission, which is essential for high-performance optoelectronics. In general, optoelectronic properties are strongly influenced by the heterojunction interface and the contact quality, and the fresh and immaculate interface in the heterostructure plays a crucial role in obtaining high responsivity [36]. Due to the characteristics of vacuum circumstance and thermal evaporation process, Cs-Cu-I grains were in tight combination with the substrates on the atomic scale. Sufficient contact may enlarge the effective interfacial contact area, which is conducive to the effective construction of heterojunction structure, and further lead to the incremental depletion layer, resulting in a more rapid carrier separation speed and higher separation efficiency [8,37].

As the uniform and flat film surface is conducive to high photodetecting capability, the compositional uniformity and morphology planeness of materials have a significant impact on the device's performance. The Raman spectra in Fig. 2(a) measured at room temperature proved that the $CsCu_2I_3$ film was successfully prepared on the GaN wafer. Moreover, the spatial Raman mapping centered at 118 cm^{-1} at different positions and the corresponding Raman spectra with similar peak positions and distances of the $CsCu_2I_3$ films also indicate the high compositional and spatial uniformity (Fig. 2(b, c)). The surface scanning electron microscope (SEM) images are shown in Fig. 2(d–g), illustrating the surface morphology and microstructure of $CsCu_2I_3$ and $Cs_3Cu_2I_5$ films on TiO_2 and GaN substrates, as well as the boundary between the films and the substrates. From the top view of the samples, it is observed that the substrates are covered with uniform and compact Cs-Cu-I grains, and the diameters of homogeneously and densely distributed nanoparticles are estimated to be 45–75 and 80–135 nm, respectively. To further illustrate the surface planeness of the evaporated Cs-Cu-I films, the surface roughness was confirmed by AFM, as depicted in Fig. 2(h–k). Intriguingly, the surface root-mean-square (RMS) roughness of TiO_2 film was 13.2 nm, while that of the evaporated $Cs_3Cu_2I_5$ film was reduced to 0.7 nm. Similarly, the RMS of the GaN substrate decreased from 5.7 to 0.6 nm after the evaporation of the $CsCu_2I_3$ film. The results above demonstrate uniform and flat Cs-Cu-I films with high purity are successfully obtained, indicating the vacuum-thermal evaporation method is a competent way to prepare high-quality films.

3.2. Electric field manipulation for enhancing photodetecting performance

Fig. 3 illustrates the time-dependent photoresponse current (*I*–*t*) curves of individual material and composite systems at 0 V bias and the comparison of their responsivity. Fig. 3(a–d) depict the inherent poor photodetecting capabilities of pure $CsCu_2I_3$ and $Cs_3Cu_2I_5$ films and the unstable performance of pure TiO_2 and GaN. The performance instability of TiO_2 mainly comes from the preparation process of solution treatment, and the current vibration of GaN may result from the poor contact between the electrode and GaN. After combining with Cs-Cu-I films, the incremental photocurrent or decremental dark current resulting from the formation of heterojunction between different materials leads to significant increases in the on/off ratios compared with individual materials, which preliminarily reveals the amelioration in photodetecting capability due to the materials combination. To quantitatively describe the improvement, we tested the responsivity-wavelength curves (Fig. 3(e, f)). The obtained responsivities were significantly larger than that of individual material, showing the optimized self-powered performance of the composite systems. Especially for the TiO_2–$Cs_3Cu_2I_5$ and GaN–$CsCu_2I_3$ systems, owing to the formation of heterojunctions and the effective manipulation of built-in electric fields on carriers, the enhancements in their self-powered performance were particularly significant. The responsivity of the TiO_2–$Cs_3Cu_2I_5$ device reached 0.29 mA W^{-1}, 7200 times that of TiO_2 (320 nm), and the GaN–$CsCu_2I_3$ device achieved a responsivity of 0.58 mA W^{-1}, 25,595 times that of GaN (340 nm). The generally increased on/off ratios and optimized sensitivities reveal the effectiveness of the built-in electric field on charge modulation and generalizability of the utilized vacuum-thermal evaporation method.

The high performance mentioned above demonstrates that GaN and $CsCu_2I_3$ got suitably integrated and their energy bands matched well. The energy band alignment is important for heterojunction structures. Based on the reported work function and bandgap [17,27], Fig. S6 presents a schematic of the energy band alignment of the type-II $CsCu_2I_3$-GaN heterojunction and the operating mechanism of the device. Generally, when materials with different Fermi levels and carrier concentration gradient contact, the spontaneous alignment of Fermi level and carrier diffusion will result in an electron depletion region (DR) under thermal equilibrium conditions, and give rise to an interfacial built-in electric field [7,38]. When incident UV light hits the surface of GaN, photons with energy equal to or exceeding the bandgap of GaN will be absorbed, and electrons will be excited from the valance band to the conduction band. Then the electron-hole pairs are induced in the GaN–$CsCu_2I_3$ heterojunction, and get separated driven by the built-in electric field. Subsequently, free electrons flow to the conduction band of GaN and then transport to the cathode, while holes move toward the valence band of $CsCu_2I_3$ and get collected by the Au anode, eventually resulting in the

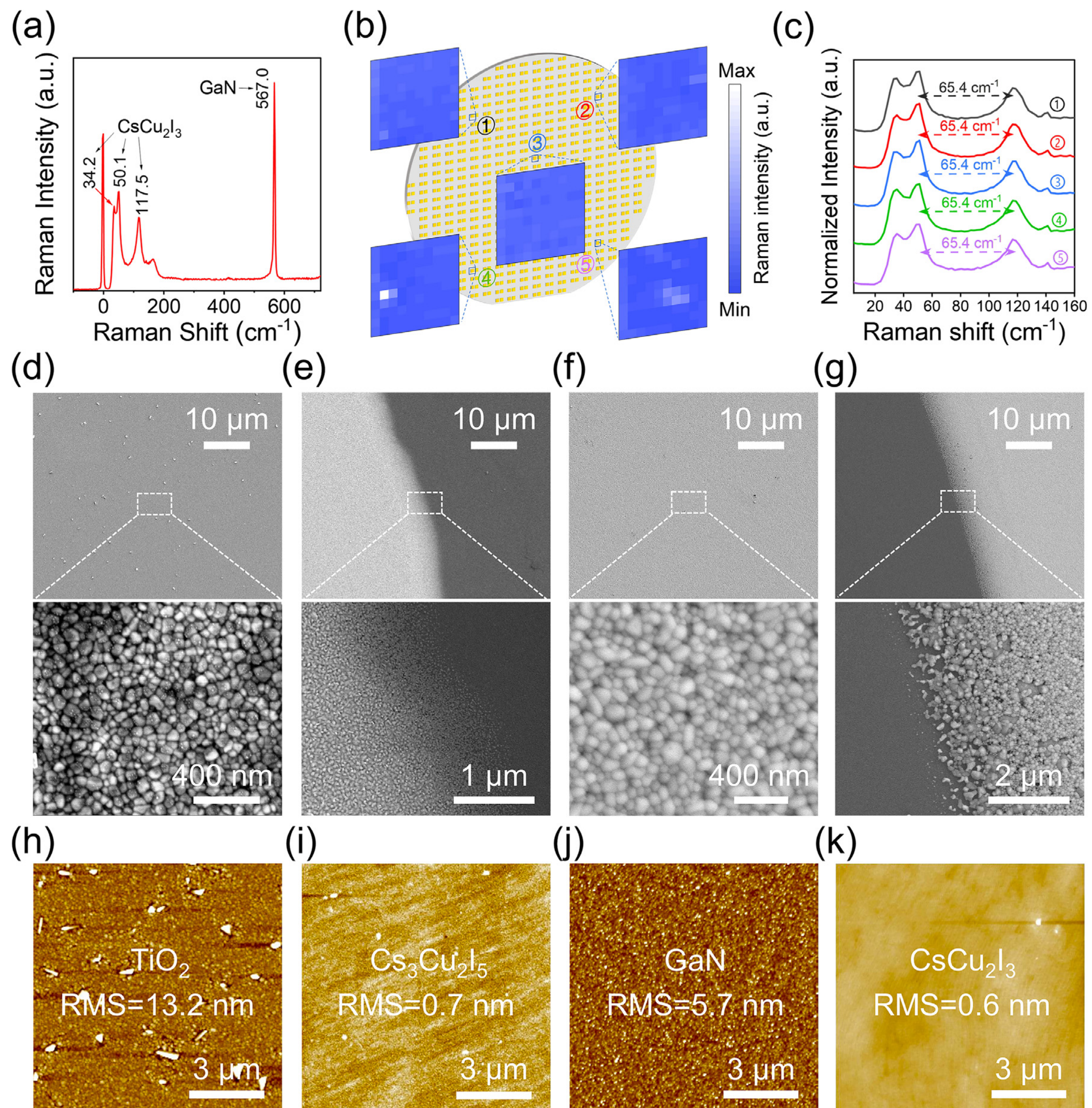

Fig. 2. Optical properties and morphology Characterizations of the Cs-Cu-I films. (a) The Raman spectra of the $CsCu_2I_3$ film on GaN. (b) Micro-area Raman mapping centered at 118 cm^{-1} for the $CsCu_2I_3$ films on the GaN. (c) The Raman spectra of $CsCu_2I_3$ films at five different points for the $CsCu_2I_3$ films on the GaN. Vertical view SEM images of (d) $CsCu_2I_3$ thin film deposited on spin-coated TiO_2 substrate, (e) the boundary between $CsCu_2I_3$ (left) and TiO_2 (right), (f) $Cs_3Cu_2I_5$ thin film deposited on spin-coated TiO_2 substrate and, (g) the boundary between $Cs_3Cu_2I_5$ (right) and TiO_2 substrate (left). AFM images of (h) spin-coated TiO_2 substrate, (i) $Cs_3Cu_2I_5$ thin film evaporated on spin-coated TiO_2 substrate, (j) GaN substrate, and (k) $CsCu_2I_3$ thin film evaporated on GaN.

photovoltaic current in the external circuit. Moreover, the built-in electric field can diminish the recombination of electron-hole pairs and inhibit the transport of electrons from GaN to $CsCu_2I_3$, which are also conducive to the lower dark current and improved detectivity.

3.3. Performance of the GaN-$CsCu_2I_3$ photodetector pixel unit

Further, the self-powered optoelectronic performances of the optimal GaN–$CsCu_2I_3$ photodetector were systematically investigated. A Schottky junction can be facilely obtained by virtue of asymmetric electrodes, and the resulting potential difference also assists to manipulate the behavior of carriers [39]. According to Fig. 4(a), the semilogarithmic *I*–*t* curve demonstrates continuous and stable on/off switching cycles. When exposed to UV light, the photocurrent of the device rose sharply and the curve immediately reached a steady state, then reduced rapidly to the dark current after removing the light source. Since no external bias is required, the dark current caused by randomly generated electrons and holes in the depletion region of heterojunction UV PDs will be smaller compared with conventional PDs. And it is noteworthy that the device simultaneously exhibited an ultra-low dark current of ~10^{-14} A and a high photocurrent of 250 nA, resulting in a terrific on/off ratio greater than 10^7, which is higher than that of pure GaN device as shown in Fig. S7. It is revealed that the built-in electric field plays different roles in discrepant conditions: it hinders charge transmission in the dark and facilitates carrier separation when illuminated. More specifically, the minimal dark current of this device arose from the large resistance in the space charge region and the suppression of majority carrier diffusion by the built-in electric field. The high photocurrent, on the other hand, was caused by the manipulation of carriers by the built-in electric field and the Schottky junction, which increased the separation efficiency of photoexcited electron-hole pairs. With such a synergistic effect of

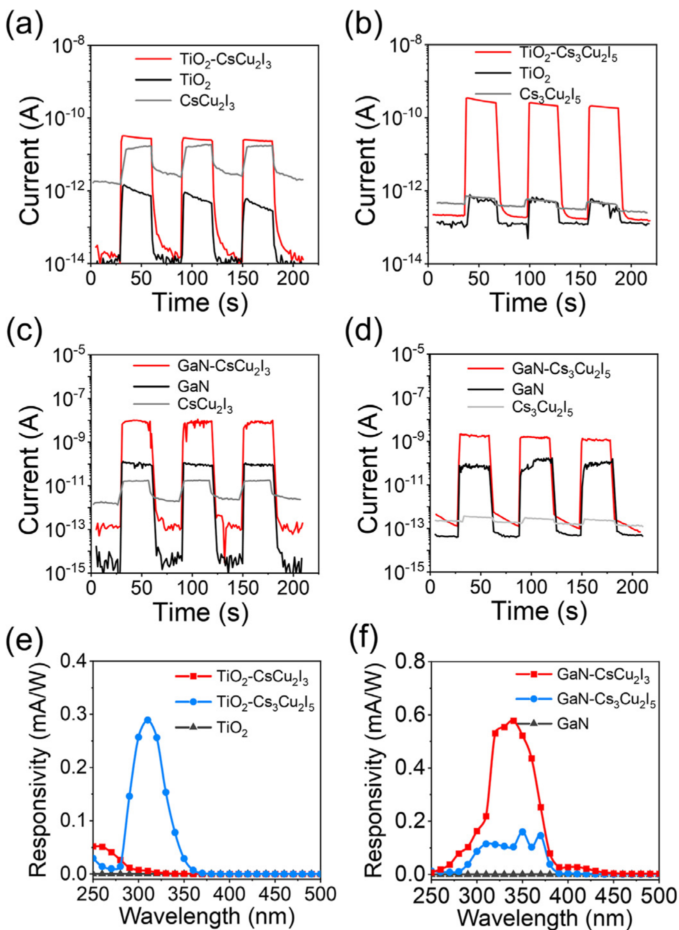

Fig. 3. Electric field manipulation by deposited Cs-Cu-I thin films. Semilogarithmic *I–t* curves under illumination on/off switching at 0 V bias of (a) TiO_2–$CsCu_2I_3$, (b) TiO_2–$Cs_3Cu_2I_5$, (c) GaN–$CsCu_2I_3$ and (d) GaN–$Cs_3Cu_2I_5$ heterostructures. Responsivity curves as a function of wavelength for photodetectors at 0 V fabricated with (e) TiO_2-based and (f) GaN-based heterostructures.

ultra-low dark current and high photocurrent, the optoelectronic performance of the device was remarkably optimized.

The responsivity (R_λ), detectivity (D^*), and external quantum efficiency (EQE) are essential parameters of a PD to evaluate the wavelength sensitivity, detection capability of faint light signals, and optoelectronic conversion efficiency [2], which can be expressed as

$$R_\lambda = \frac{I_p - I_d}{P_\lambda \cdot S}$$

$$D^* = \frac{R_\lambda}{(2eI_d/S)^{1/2}}$$

$$\mathrm{EQE} = \frac{hc}{e}\frac{R_\lambda}{\lambda} \quad (3)$$

where h, e, and c denote the Plank constant, the elemental charge, and the velocity of light. And I_p and I_d represent the photocurrent and the dark current. S is the effective illumination area and P_λ is the light power density. The photocurrents of the device were measured under the illumination of monochromatic light with wavelength changing from 250 to 400 nm at 0 V bias (Fig. S8), and the responsivity, detectivity, and EQE were calculated to evaluate its photodetecting capability. As can be observed in Fig. 4(b), the device demonstrated a filterless narrowband photoresponse with a full width at half-maximum (FWHM) as narrow as 18 nm. And the UV–visible rejection ratio ($R_{350\ nm}$ / $R_{400\ nm}$) was calculated to be 262, which also confirmed the excellent wavelength selectivity in the UV region. This is of great significance since there are few reports on narrowband perovskite-based UV PDs that are highly desired for certain optical applications, like selected-wavelength imaging and chemical element detection. When light hits an object, the shorter the wavelength of the light, the more easily it will be absorbed and the shorter its depth of penetration will be. Due to the limited diffusion length of carriers induced by deep UV light, electrons generated in regions far from the depletion layer will recombine and cannot be collected by electrodes. Meanwhile, the UV light of ~350 nm can penetrate deeper into films owing to less absorption, and photogenerated carriers can diffuse to the depletion layer and be further separated and collected, resulting in high spectral selectivity [17]. Due to the strong response only to a special spectral range of about 350 nm, the GaN–$CsCu_2I_3$ structure can be a promising candidate for high spectrum-selectivity UV PDs and UV imaging devices.

Additionally, the R and D^* of the device reached maxima of 256 mA W^{-1} and 2.16 × 10^{13} cm $Hz^{1/2}$ W^{-1} (Jones) under 350 nm illumination, respectively. And the EQE reached 91.0% as shown in Fig. S9. The demonstrated self-powered photodetecting performance is better than most existing heterojunction UV PDs and lead-free perovskite-containing UV PDs (Table S1). And there is a comparison of the detectivity and on/off ratio between the GaN–$CsCu_2I_3$ PD and some other reported self-powered PDs in Fig. 4(h). The enhanced responsivity and detectivity could be ascribed to the rationally designed built-in electric field in the heterojunction, which is caused by the favorable energy band alignment. And the vacuum evaporation method entitles $CsCu_2I_3$ film and GaN–$CsCu_2I_3$ interface with satisfactory crystal quality and decent interfacial properties, respectively. On the one hand, semiconductors with high crystal quality have fewer defects and grain boundaries, which is conducive to the separation and transportation process of photogenerated carriers [14]. On the other hand, the competent interfacial properties of GaN–$CsCu_2I_3$ and sufficient contact between them further reduce the number of defects at the interface, leading to incremental carrier extraction and less non-radiative recombination at defects or induced traps [11]. As a consequence of the efficient interfacial carrier separation and suppressed recombination, more separated electrons and holes will flow to the cathode and anode respectively, and the number and lifetime of carriers will be increased and prolonged, eventually leading to the enhanced photocurrent (approaching the μA level) and high responsivity. Coupled with the spontaneous advantage of ultra-low dark current of the built-in electric field manipulation, exceptional detectivity was also realized.

It is well-known that the photogeneration probability of charge carriers is proportional to the absorbed photon flux. And the photocurrent is delineated as a power function of photodensity $I = \alpha P^\theta$, where α is a constant under a certain wavelength, and θ is a parameter related to the recombination process of the photogenerated carriers. The photosensitivity of the GaN–$CsCu_2I_3$ device was also tested under 350 nm UV light with different light power densities ranging from 12.1 to 2272 μW cm^{-2} (Fig. S10). It can be seen that the photocurrent got increased as the light power density rises, and the device exhibited obvious rectification characteristics. The rectification ratios maintained greater than 10^2 (± 1 V) not only under the illumination of different photodensities at 350 nm but also at different wavelengths of 250–400 nm UV, as depicted in Fig. S12. These rectification behaviors are generally deduced to originate from the heterojunction structure [2]. The photocurrent remained essentially constant over the bias range of 0 to –1 V (Fig. S12(a)), revealing that the built-in electric field was strong enough so that the photogenerated carriers can be completely collected by the built-in electric field regardless of the external bias. This is of great significance for practical applications, as the constant photocurrent within this operating bias range would prevent interfer-

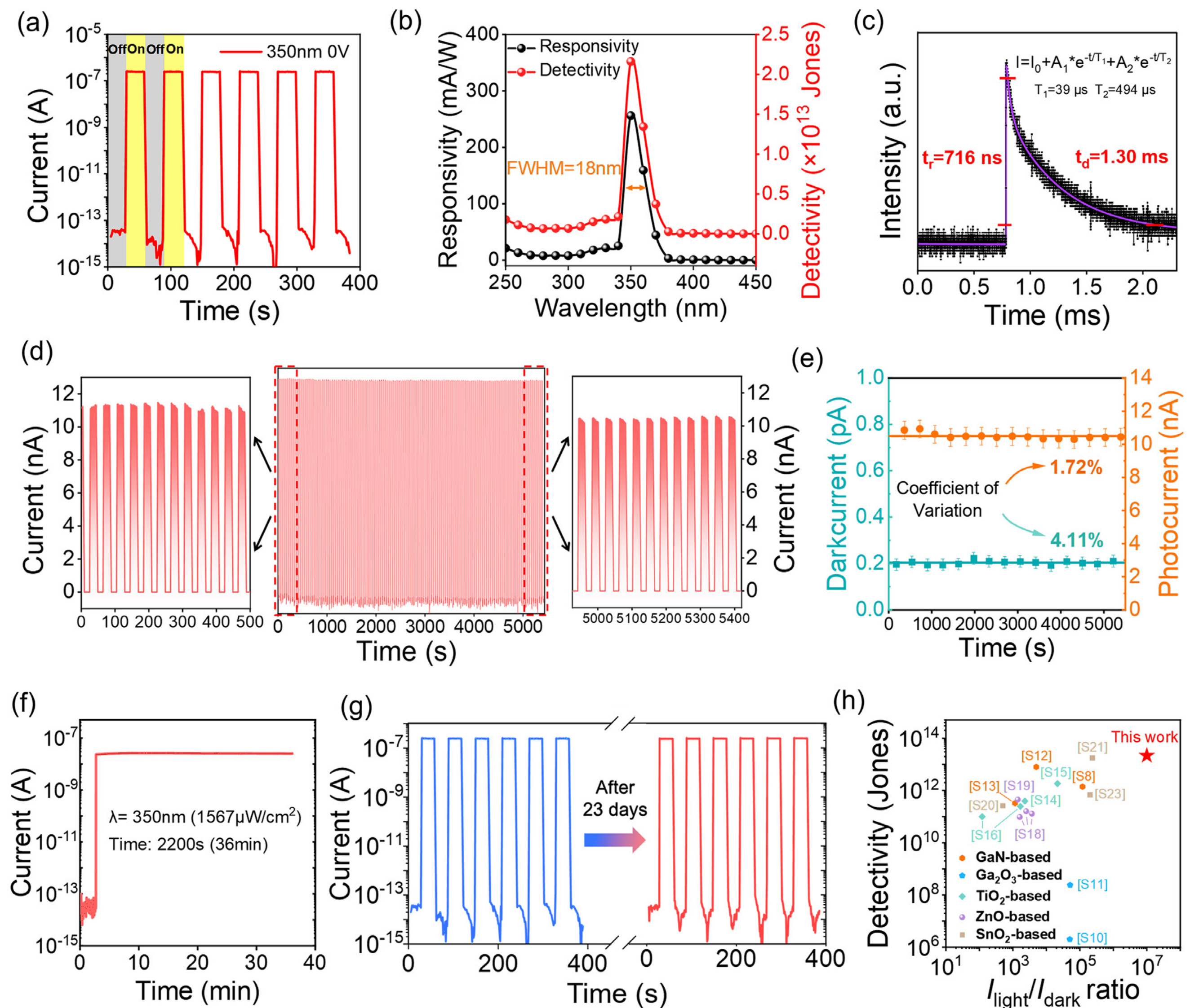

Fig. 4. Optoelectronic performances of GaN–$CsCu_2I_3$ heterostructure photodetector unit. (a) Semilogarithmic *I–t* curve under on/off switching 350 nm illumination at 0 V bias. (b) Responsivity and detectivity curves as a function of wavelength at 0 V bias. (c) Time-resolved photoresponse under 10 Hz 355 nm laser pulse at 0 V bias. Rise and decay time is defined as the time switching between 10% and 90% of the maximum photocurrent. (d) A total of 135 continuous response cycles of the device, illuminating with a hand-held 365 nm UV lamp. (e) The coefficients of variation of dark/photo- current calculated from randomly selected 15 data points. (f) *I–t* curve of 2200s continuous operation under 350 nm illumination at 0 V bias. (g) Long-term stability in ambient air. (h) Comparison of on-off ratio and detectivity with those of reported self-powered photodetectors based on wide-bandgap semiconductor/perovskite heterostructure.

ence with signal intensity caused by voltage fluctuations. At the bias of −1, 0, and 1 V, the photocurrent values corresponding to different photodensities were taken, and curves of the photocurrent as a function of photodensity were made (Fig. S11). By fitting the curves with the power-law equation, the values of best-fitting power indexes θ were calculated to be 1.12, 0.93, and 0.85 at −1, 0, and 1 V bias, respectively. The nonunity indexes of the law are considered to be related to the complex processes of the carriers' generation, trapping, and recombination in the device [40]. Furthermore, the suitable linear-like relationship (θ = 0.93) at 0 V bias disclosed that the device is closer to an ideal device (θ = 1) with little recombination loss, which is highly desired for the practical use of sensors.

In addition to low dark current, the fast response is another advantage of heterojunction structure UV PDs [4]. The transient response time was measured under the excitation of the 355 nm pulse laser with 10 Hz frequency and 0 V bias, as shown in Fig. 4(c). The response speed of a PD is mainly related to the transmission and collection process of charge. And generally, due to the relatively long carrier lifetime resulting from defect concentration and ion shielding effect, perovskite-based photodetectors possess long photoresponse time [7]. However, as Fig. 4(c) illustrates, the amplified and normalized *I–t* curves elucidated the ultrafast photoresponse speed of the device. The decay time can be fitted by the equation: $I = I_0 + A_1 \cdot e^{-t/T}{}_T + A_2 \cdot e^{-t/T}{}_T$. And the rise time t_r and decay time t_d were evaluated to be 716 ns and 1.30 ms. Compared with other typical photodetectors in Table S1, it is evident that this device possesses a much faster response speed, especially the outstanding rise time of the nanosecond level represents the optimal response speed of most self-powered perovskite PDs at present. This ultrafast photoresponse characteristic may originate from the instantaneous and efficient charge separation caused by the type-II heterojunction structure and the drift process of minority carriers in the junction region. When the incident photons are absorbed, the built-in electric field in the heterojunction will provide a strong driving force and separate the carriers at a very fast rate, resulting in a dramatic reduction in the rise time. Once the light is removed, the electrons from GaN recombine with holes from $CsCu_2I_3$

at the interface, and the depletion layer will instantly stop the transportation of carriers [4]. There is a big difference between t_r and t_d. It is considered that the single-crystalline structure of GaN and the built-in electric field effectively boost the photoresponse, while defects at the heterojunction interface may affect the recombination process of electrons and holes, resulting in a slower decay time.

Just as the instability of conventional lead-halide perovskites seriously inhibits their further development, the stability of a photodetector, including continuous operational stability and long-term stability, plays a significant role in its future applications. Herein, the consecutive *I–t* curve of multiple cycles was tested, and the dynamic response of the self-powered PD exhibited excellent switching stability and duplicability. As Fig. 4(d) illustrates, there was no obvious attenuation of photocurrent and both photo-/dark currents remained stable throughout the testing process, which revealed the great operational stability of the device. To better illustrate this point, 15 dark current data and 15 photocurrent data were selected at 360 s intervals from the whole process, and their coefficients of variation (C_V) were calculated, which can be expressed by the following formula:

$$C_V = \frac{|\sigma|}{\mu} = \frac{\sqrt{\frac{1}{N}\sum_{i=1}^{N}(X_i - \mu)}}{\frac{1}{N}\sum_{i=1}^{N}X_i} \tag{4}$$

where σ and μ are the standard deviation and mean value of all data. As shown in Fig. 4(e), the C_V of dark current and photocurrent were 4.11% and 1.72%, respectively, which reveals the negligible alterations throughout the process. Furthermore, the photocurrent of the device did not show any attenuation even after being illuminated for more than 35 min as Fig. 4(f) reveals. Long-term stability is another critical factor for practical application. As shown in Fig. 4(g), the *I–t* curve of the unencapsulated and unprotected device was tested again after being placed in air for more than 23 days. Benefiting from the decent structural and chemical stability of GaN and $CsCu_2I_3$, the photocurrent remains virtually unchanged, also demonstrating excellent long-term storage stability.

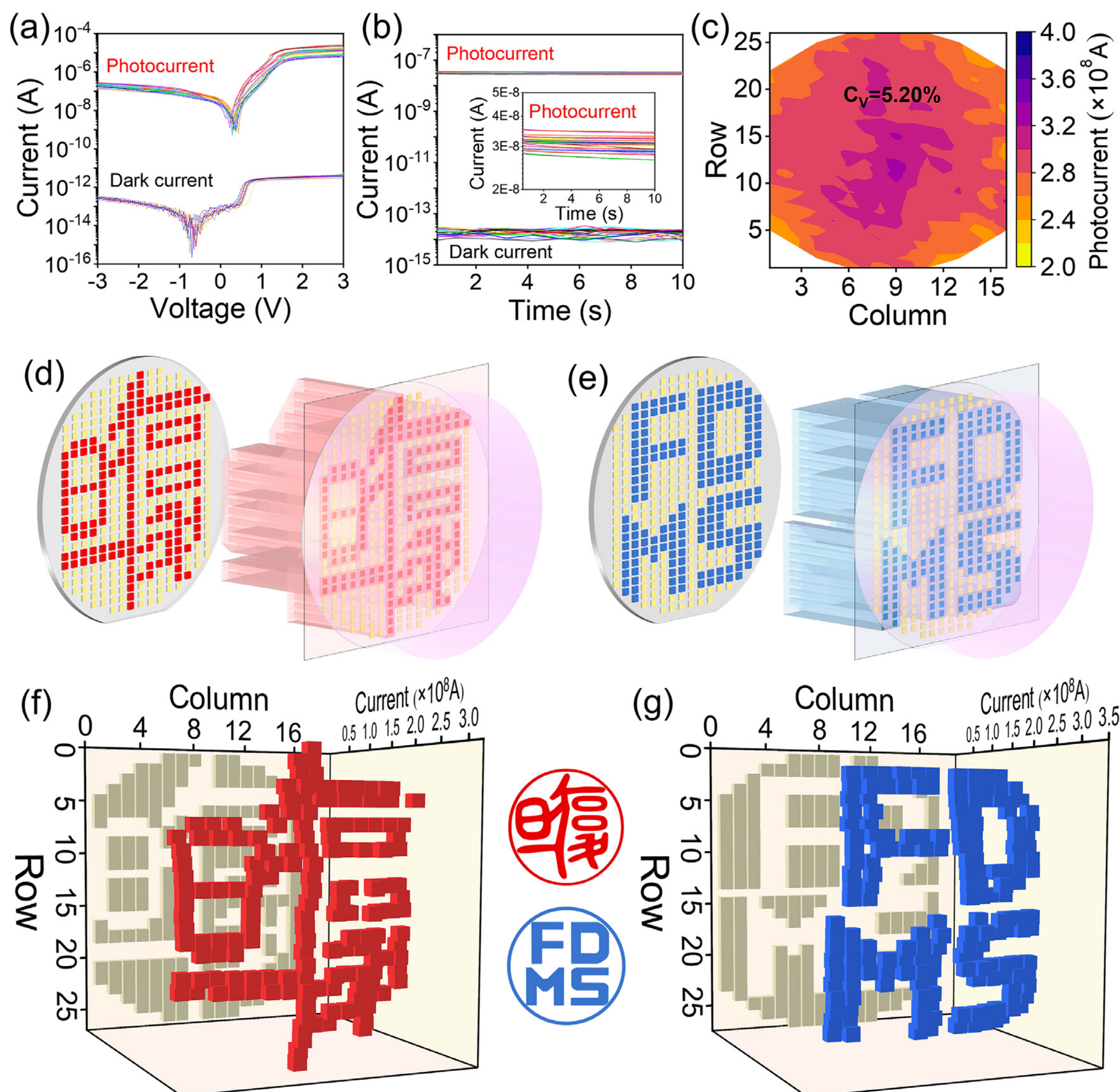

Fig. 5. High-performance UV imaging sensor based on the integrated PDs. (a) Statistical *I–V* curves of randomly selected illuminated and unilluminated units. (b) Statistical *I–t* curves of devices in the 9th row of the array under 350 nm UV illumination and non-illumination conditions at 0 V bias. The inset shows the *I–t* curves with an amplified current axis. (c) Photocurrent mapping of the 372-pixel GaN–$CsCu_2I_3$ photodetector array. (d, e) Schematic illustrations for the simulated imaging process, the differences between the photocurrents and dark currents of the illuminated and unilluminated lead to contrasts. (f, g) The actual imaging results formed by the contrasts of the corresponding photocurrents and dark currents measured under 350 nm illumination at 0 V bias, with different patterns of the emblem of Fudan University and the letters “FDMS”.

3.4. A 372-pixel imaging sensor

As mentioned before, the vacuum-thermal evaporation method has shown great advantages in producing uniform and flat films with high-quality and manufacturing integrated large-scale array devices. This is of great significance since the large-scale integrations of heterojunction UV PDs which demands mature technology and reliable heterojunctions are hard to be realized [29]. And analogous photoresponse properties, especially the photocurrents with very small discrepancies, are the prerequisite for achieving high-quality imaging functionality. Meanwhile, considering the high demand for imaging sensors for low dark current and high on/off ratio, the device fabricated by the vacuum-thermal evaporation method in this work is perfectly suitable to function as sensor pixels. Its ultra-high on/off ratio allows the sensor to produce more sub-dividable signal intensities for light with different photodensities (e.g. each of the 0–255 gray-level can represent a wider signal interval), entitling the imaging results with greater contrast and resolution. Furthermore, the ultra-fast photoresponse speed and narrowband photoresponse property would endow the imaging sensor with a high frame rate and the capability to respond only to a specific wavelength (350 nm) without interference from other wavelengths of light.

Herein, a 2-inch GaN wafer substrate was introduced to fabricate an imaging array consisting of 372 devices (26 rows and 16 columns, i.e. R26 & C16) with identical structures. Note the influence of preparation defects and performance discrepancies between the edge and the middle of the GaN wafer, we randomly selected a number of device units for *I–V* tests and found that these measured curves were generally consistent, as shown in Fig. 5(a). Then, the photocurrents and dark currents of pixel devices in the 9th column (26 devices in total) were tested at 0 V bias. Fig. 5(b) indicates that the currents, especially the photocurrents of the 26 devices are very close to each other. The mean value and C_V were 3.0×10^{-8} A and 5.48% for photocurrents, and 2.1×10^{-14} A and 15.6% for dark currents, preliminarily revealing the high homogeneity of the integrated device. The photocurrent of each GaN–$CsCu_2I_3$ unit was measured under 350 nm illumination (1567 μW cm^{-2}) at 0 V. The photocurrent mapping of the whole integrated device is shown in Fig. 5(c). It is obvious that all photocurrents show tiny discrepancies (the C_V is calculated to be only 5.20%), demonstrating satisfactory electrical homogeneity (Fig. S13). It should be pointed out that the photocurrent in the middle area of the array is relatively high, which is originate from the thinner thickness of the middle GaN substrate itself. To demonstrate the imaging capability using vacuum-evaporated $CsCu_2I_3$ films, a GaN device array was prepared on the same GaN substrate (Fig. S14). In contrast, the photocurrents of the pure GaN array exhibited large variations, with a C_V as high as 89.0% (Fig. S15). These results indicate the outstanding electrical homogeneity of the fabricated imaging array, and the evaporated films are also proved to improve the non-uniformity of the properties caused by the surface roughness and defects of the substrate, which demonstrates the substrate-independent nature and the superiority of the vacuum thermal evaporation technique in large-scale imaging sensors.

To exhibit the imaging functionality, the sensor is imaged using a light spot with the selected pixel. As shown in Fig. 5(d, e), there will be a contrast between illuminated and unilluminated pixels, which is reflected in the level of currents. Consequently, it can ultimately project the desired patterns based on the photocurrent distribution, i.e. the emblem of Fudan University and the letters “FDMS” shown in the insets between Fig. 5(f, g). The pixels participating in imaging are shown in Fig. S16. These results manifest that the patterns can be presented clearly even when applying linear current coordinates, revealing the high recognition due to the outstanding homogeneity of the imaging sensor and remarkable photocurrent response of the devices, which originates from the ascendancy of the evaporation process and the construction of heterojunction, respectively. In contrast, the imaging quality and resolution of the GaN device array are much worse (Fig. S17), and clear imaging cannot be obtained even if using logarithmic current coordinates. It should be pointed out that the imaging resolution of a sensor is usually restricted by the size and inhomogeneity of pixels. By dwindling the channel and taking full advantage of the micro-size of the device, such as introducing photolithography technology and exploring the possibility of constructing the vertical structure GaN–$CsCu_2I_3$ device, it is promising to achieve further improvements in pixel intensity and array resolution, and further integrating the device with state-of-the-art CMOS and TFT technologies. Totally, this research presents a vacuum-deposited method to realize the heterogeneous integration of large-scale photodetectors with high homogeneity, which is significant to highly integrated and high-density optoelectronic systems, such as electronic-eyes and high-speed cameras.

4. Conclusion

Wafer-scale Cs-Cu-I films have been successfully prepared via vacuum-thermal evaporation technology, and heterojunction UV PDs are fabricated. The vacuum evaporation process entitles the nanoscale Cs-Cu-I films with homogeneous and compact morphologies, endowing the heterojunction structure with excellent interface properties and providing significant performance enhancement for the UV PDs. The optimal GaN–$CsCu_2I_3$ photodetector reveals an ultrahigh on/off ratio greater than 10^7, a remarkable responsivity up to 256 mA W^{-1}, and a detectivity of 2.16×10^{13} cm $Hz^{1/2}$ W^{-1} under 350 nm UV light illumination at 0 V bias. The impressive photodetecting performance is attributed to the effective manipulation of carrier transportation by the built-in electric field in the heterojunction. And the resulting effective charge separation and prolonged carrier lifetime realize a balance between high responsivity and fast photoresponse speed of the device. The UV PD also exhibits an ultrafast photoresponse speed (t_r = 716 ns, t_{dv}= 1.30 ms at 0 V bias) and outstanding stability. Moreover, the as-constructed 372-pixel imaging sensor reveals outstanding electrical uniformity and satisfactory imaging functionality, demonstrating the noteworthy prospect of the vacuum-thermal evaporation technique for the large-scale integration of metal halide perovskites and wide-bandgap semiconductors for future optoelectronic devices.

Declaration of Competing Interest

The authors declare that they have no known competing financial interests or personal relationships that could have appeared to influence the work reported in this paper.

Acknowledgements

This work was financially supported by the National Natural Science Foundation of China (Nos. 92263106, 62204047, and 12061131009), Science and Technology Commission of Shanghai Municipality (Nos. 21520712600 and 19520744300).

Supplementary materials

Supplementary material associated with this article can be found, in the online version, at doi:10.1016/j.jmst.2023.05.007.

References

[1] Y. Kim, J.M. Suh, J. Shin, Y.P. Liu, H. Yeon, K. Qiao, H.S. Kum, C. Kim, H.E. Lee, C. Choi, H. Kim, D. Lee, J. Lee, J.-H. Kang, B.-I. Park, S. Kang, J. Kim, S. Kim, J.A. Perozek, K. Wang, Y. Park, K. Kishen, L. Kong, T. Palacios, J. Park, M.-C. Park, H.-J. Kim, Y.S. Lee, K. Lee, S.-H. Bae, W. Kong, J. Han, J. Kim, Science 377 (2022) 859–869.
[2] X. He, M. Wang, F.R. Cao, W. Tian, L. Li, J. Mater. Sci. Technol. 124 (2022) 243–251.
[3] J.C. Zhang, P.F. Dong, K. Dang, Y.N. Zhang, Q.L. Yan, H. Xiang, J. Su, Z.H. Liu, M.W. Si, J.C. Gao, M.F. Kong, H. Zhou, Y. Hao, Nat. Commun. 13 (2022) 3900.
[4] Z.L. Li, Z.Q. Li, C.L. Zuo, X.S. Fang, Adv. Mater. 34 (2022) 2109083.
[5] Y.H. Chen, L.X. Su, M.M. Jiang, X.S. Fang, J. Mater. Sci. Technol. 105 (2022) 259–265.
[6] W.D. Song, J.X. Chen, Z.L. Li, X.S. Fang, Adv. Mater. 33 (2021) 2101059.
[7] F. Wang, X.M. Zou, M.J. Xu, H. Wang, H.L. Wang, H.J. Guo, J.X. Guo, P. Wang, M. Peng, Z. Wang, Y. Wang, J.S. Miao, F.S. Chen, J.L. Wang, X.S. Chen, A.L. Pan, C.X. Shan, L. Liao, W.D. Hu, Adv. Sci. 8 (2021) 2100569.
[8] X. Zhang, J. Grajal, J.L. Vazquez-Roy, U. Radhakrishna, X.X. Wang, W. Chern, L. Zhou, Y.X. Lin, P.-C. Shen, X. Ji, X. Ling, A. Zubair, Y. Zhang, H. Wang, M. Dubey, J. Kong, M. Dresselhaus, T. Palacios, Nature 566 (2019) 368–372.
[9] W.X. Ouyang, J.X. Chen, Z.F. Shi, X.S. Fang, Appl. Phys. Rev. 8 (2021) 031315.
[10] C. Lan, H. Zou, L. Wang, M. Zhang, S. Pan, Y. Ma, Y. Qiu, Z.L. Wang, Z. Lin, Adv. Mater. 32 (2020) 2005481.
[11] O. Voznyy, B.R. Sutherland, A.H. Ip, D. Zhitomirsky, E.H. Sargent, Nat. Rev. Mater. 2 (2017) 17026.
[12] D.H. Wang, X. Liu, Y. Kang, X.N. Wang, Y.P. Wu, S. Fang, H.B. Yu, M.H. Memon, H.C. Zhang, W. Hu, Z.T. Mi, L. Fu, H.D. Sun, S.B. Long, Nat. Electron. 4 (2021) 645–652.
[13] D. Hao, D. Liu, Y. Shen, Q. Shi, J. Huang, Adv. Funct. Mater. 31 (2021) 2100773.
[14] F.R. Cao, L. Li, Adv. Funct. Mater. 31 (2020) 2008275.
[15] E. Hong, Z.Q. Li, T. Yan, X.S. Fang, Nano Lett. 22 (2022) 8662–8669.
[16] X.T. Wu, W.D. Song, Q. Li, X.X. Zhao, D.S. He, Z.W. Quan, Angew. Chem. Int. Edit. 59 (2020) 1030–1046.
[17] Y. Li, Z.F. Shi, W.Q. Liang, L.T. Wang, S. Li, F. Zhang, Z.Z. Ma, Y. Wang, Y.Z. Tian, D. Wu, X.J. Li, Y.T. Zhang, C.X. Shan, X.S. Fang, Mater. Horizons 7 (2020) 530–540.
[18] Y. Zhang, Y. Ma, Y. Wang, X. Zhang, C. Zuo, L. Shen, L. Ding, Adv. Mater. 33 (2021) 2006691.
[19] Z.Q. Li, Z.L. Li, Z.F. Shi, X.S. Fang, Adv. Funct. Mater. 30 (2020) 2002634.
[20] Z.Q. Li, X.Y. Liu, C.L. Zuo, W. Yang, X.S. Fang, Adv. Mater. 33 (2021) 2103010.
[21] P. Liu, Y. Liu, S.W. Zhang, J.Z. Li, C.Y. Wang, C. Zhao, P.B. Nie, Y.H. Dong, X. Zhang, S.X. Zhao, G.D. Wei, Adv. Opt. Mater. 8 (2020) 2001072.
[22] L.J. Dai, Z.Y. Deng, F. Auras, H. Goodwin, Z.L. Zhang, J.C. Walmsley, P.D. Bristowe, F. Deschler, N.C. Greenham, Nat. Photon. 15 (2021) 696–702.
[23] D.X. Yang, G.L. Zhang, R.C. Lai, Y. Cheng, Y.X. Lian, M. Rao, D.X. Huo, D.C. Lan, B.D. Zhao, D.W. Di, Nat. Commun. 12 (2021) 4295.
[24] P.F. Cheng, L. Sun, L. Feng, S.Q. Yang, Y. Yang, D.Y. Zheng, Y. Zhao, Y.B. Sang, R.L. Zhang, D.H. Wei, W.Q. Deng, K. Han, Angew. Chem. Int. Edit. 58 (2019) 16087–16091.
[25] M.Y. Zhang, J.S. Zhu, B. Yang, G.D. Niu, H.D. Wu, X. Zhao, L.X. Yin, T. Jin, X.Y. Liang, J. Tang, Nano Lett. 21 (2021) 1392–1399.
[26] K.J. Kwak, J.H. Baek, D.E. Lee, I.H. Im, J. Kim, S.J. Kim, Y.J. Lee, J.Y. Kim, H.W. Jang, Nano Lett. 22 (2022) 6010–6017.
[27] H. Chen, L. Zhu, C. Xue, P.L. Liu, X.R. Du, K.C. Wen, H. Zhang, L. Xu, C.S. Xiang, C. Lin, M.C. Qin, J. Zhang, T. Jiang, C. Yi, L. Cheng, C.L. Zhang, P.H. Yang, M.L. Niu, W.J. Xu, J.Y. Lai, Y. Cao, J. Chang, H. Tian, Y.Z. Jin, X.H. Lu, L. Jiang, N.N. Wang, W. Huang, J.P. Wang, Nat. Commun. 12 (2021) 1421.
[28] C. Zou, Q. Liu, K. Chen, F. Chen, Z. Zhao, Y. Cao, C. Deng, X. Wang, X. Li, S. Zhan, F. Gao, S. Li, Mater. Horizons 9 (2022) 1479–1488.
[29] C. Li, W.C. Huang, L.F. Gao, H.D. Wang, L.P. Hu, T.T. Chen, H. Zhang, Nanoscale 12 (2020) 2201–2227.
[30] Y.H. Li, K.S. Yang, Chem. Soc. Rev. 45 (2016) 655–689.
[31] K. Dong, H. Zhou, W. Shao, Z. Gao, F. Yao, M. Xiao, J. Li, Y. Liu, S. Wang, S. Zhou, H. Cui, M. Qin, X. Lu, C. Tao, W. Ke, G. Fang, ACS Nano 17 (2023) 1495–1504.
[32] X.Y. Zhou, L.C. Zhang, Y. Huang, Z.Y. Zhou, W.Q. Xing, J. Zhang, F.W. Zhou, D.Y. Zhang, F.Z. Zhao, Adv. Opt. Mater. 9 (2021) 2100889.
[33] S.Y. Hsiao, H.L. Lin, W.H. Lee, W.L. Tsai, K.M. Chiang, W.Y. Liao, C.Z. Ren-Wu, C.Y. Chen, H.W. Lin, Adv. Mater. 28 (2016) 7013–7019.
[34] P.P. Du, J.H. Li, L. Wang, L. Sun, X. Wang, X. Xu, L.B. Yang, J.C. Pang, W.X. Liang, J.J. Luo, Y. Ma, J. Tang, Nat. Commun. 12 (2021) 4751.
[35] K.L. Liu, B. Fin, W. Han, X. Chen, P.L. Gong, L. Huang, Y.H. Zhao, L. Li, S.J. Yang, X.Z. Hu, J.Y. Duan, L.X. Liu, F.K. Wang, F.W. Zhuge, T.Y. Zhai, Nat. Electron. 4 (2021) 906–913.
[36] X. Hu, X.Y. Li, G.Y. Li, T. Ji, F.J. Ai, J.H. Wu, E.N. Ha, J.Q. Hu, Adv. Funct. Mater. 31 (2021) 2011284.
[37] F. Cao, Z.Q. Li, X.Y. Liu, Z.F. Shi, X.S. Fang, Adv. Funct. Mater. 32 (2022) 2206151.
[38] Z.S. Luo, X.Y. Ye, S.J. Zhang, S.K. Xue, C. Yang, Y.D. Hou, W.D. Xing, R. Yu, J. Sun, Z.Y. Yu, X.C. Wang, Nat. Commun. 13 (2022) 2230.
[39] F.W. Guo, B. Yang, Y.B. Yuan, Z.G. Xiao, Q.F. Dong, Y. Bi, J.S. Huang, Nat. Nanotechnol. 7 (2012) 798–802.
[40] R. Saran, R.J. Curry, Small 14 (2018) 1703624.